The validity of Monte Carlo simulation in studies of scattered radiation in diagnostic radiology

Article *in* Physics in Medicine and Biology · March 1983

DOI: 10.1088/0031-9155/28/2/001 · Source: PubMed

2 authors:

Heang-Ping Chan
University of Michigan
575 PUBLICATIONS **15,474** CITATIONS
SEE PROFILE

Kunio Doi
University of Chicago
736 PUBLICATIONS **24,054** CITATIONS
SEE PROFILE

The validity of Monte Carlo simulation in studies of scattered radiation in diagnostic radiology

Phys. Med. Biol., 1983, Vol. 28, No. 2, 109–129. Printed in Great Britain

The validity of Monte Carlo simulation in studies of scattered radiation in diagnostic radiology

Heang-Ping Chan and Kunio Doi

The Kurt Rossmann Laboratories for Radiologic Image Research, Department of Radiology, The University of Chicago, 950 East 59th Street, Chicago, IL 60637, USA

Received 13 April 1982, in final form 26 June 1982

Abstract. A computer program using Monte Carlo methods has been developed for the simulation of photon scattering in tissue-equivalent phantoms for incident X-rays in the diagnostic energy range. The study verified that the sampling schemes used in the program can produce random samples according to the theoretical probability distribution functions which describe the photon-scattering process. The Monte Carlo program was applied to determinations of the scatter fractions and edge responses for various phantom sizes, X-ray energies, and recording systems. These quantities were also measured experimentally under comparable imaging conditions. Excellent agreement was obtained between the predicted and experimental results. This investigation established the validity of our Monte Carlo calculations for studies of the physical characteristics of scattered radiation in diagnostic radiology.

1. Introduction

One of the important factors affecting radiographic image quality is the scattered radiation arising from interaction of the photons with the object being radiographed. The large amount of scattered radiation results in reduction of image contrast. In order to devise an effective antiscatter technique for a radiographic procedure, one must have a thorough understanding of the physical characteristics of the scattered radiation. Up to now, very limited experimental data have been published regarding important properties such as the scatter fraction, angular distribution, and spectral distributions of the scattered radiation under diagnostic imaging conditions (Wilsey 1921, Hettinger and Starfelt 1959, Hettinger and Liden 1960, Reiss and Steinle 1973, Motz and Dick 1975, Dick *et al* 1978, Strid 1976, Barnes *et al* 1976, Levine and Hale 1980, Burgess and Pate 1981).

Theoretical investigation of the properties of scattered radiation has also been attempted; however, in analytical approaches multiple scattering processes are inevitably neglected. Monte Carlo calculation is by far the most successful method for the simulation of the stochastic process of particle transport in a scattering medium. Koblinger and Zarand (1973) performed a Monte Carlo simulation study of photon scattering in chest radiography. A more extensive calculation of organ dose with Monte Carlo methods was carried out by Rosenstein *et al* (1976) for various diagnostic procedures. Dance (1980) applied Monte Carlo methods to predict the integral radiation dose to the breast in xeromammography. These authors, however, concentrated on determining the dose distribution in the organs during the radiographic examination. Other important characteristics of scattered radiation were not considered. Reiss and Steinle (1973) used Monte Carlo calculations to investigate the

0031-9155/83/020109+21$02.25

physical properties of scattered radiation under diagnostic imaging condition. Their results comprise the first extensive data on the angular and spectral distributions of scattered radiation in diagnostic radiology. However, they did not consider the effect of the energy response of recording systems on the detection of scattered radiation. More recently, Kalender (1981) employed Monte Carlo simulation to calculate scatter data for some diagnostic imaging conditions; however, he emphasised the scatter fractions without providing detailed information on other important properties.

We have conducted a comprehensive investigation of the imaging properties of scattered radiation in diagnostic radiology by means of Monte Carlo calculations (Chan 1981). Here, we will describe the Monte Carlo photon transport program for the simulation of photon scattering in a homogeneous tissue-equivalent phantom. We applied the program to determine scatter fractions and the spatial distribution of the scattered radiation emerging from a Lucite (methyl methacrylate $(C_5H_8O_2)_n$, also known as Plexiglas or Perspex) phantom onto the image plane for various phantom sizes, incident energies, and screen–film systems. The predicted results were compared with experimental measurements performed under similar conditions for verification of the validity of our Monte Carlo calculations. These comparisons establish the basis of applying the program to the study of the various physical properties of scattered radiation (Chan 1981) which will be published elsewhere.

2. Description of the Monte Carlo program

A schema of our Monte Carlo code for photon diffusion in tissue-equivalent phantoms is shown in figure 1. In the diagnostic energy range, three interaction processes—the

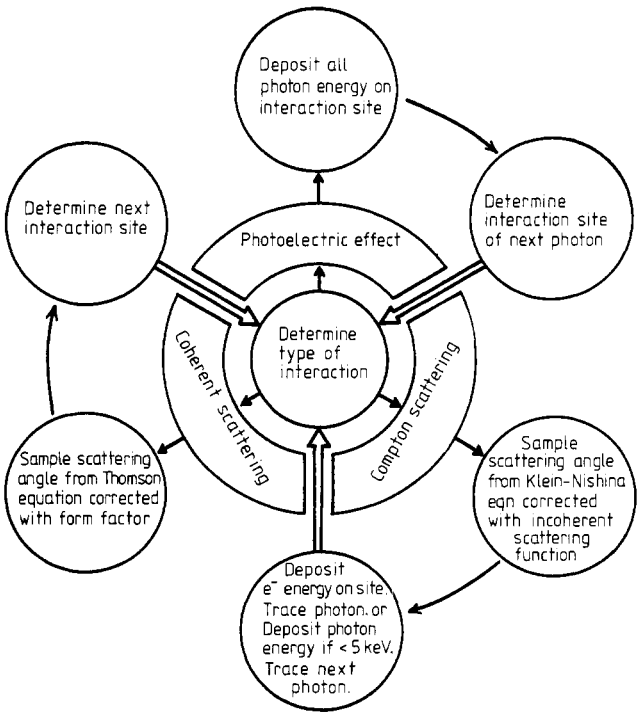

Figure 1. Schema of a computer program for the simulation of photon transport in a scattering medium by Monte Carlo methods.

photoelectric effect, coherent scattering, and incoherent scattering—have to be considered. An x-ray photon impinges on the surface of the phantom. The incident energy of the photon is determined from the energy distribution of the x-ray spectrum. Its initial direction is chosen based on the spatial distribution of the x-ray beam. The entry point is calculated according to the geometry of the irradiation. We will describe in the following sections the essential features of the methods we used for tracing photon histories in the phantom. A more detailed discussion can be found in the work by Chan (1981).

2.1. Determination of free path length

The free path length ρ of the photon is obtained by a random sampling with an inversion method† from the exponential probability density function (PDF) of ρ:

$$p(\rho) = \mu\, e^{-\mu\rho} \tag{1}$$

such that $\rho = (1/\mu) \ln \xi$, where ξ is a random number uniformly distributed in the interval $(0, 1]$ and μ is the total linear attenuation coefficient of the scattering medium at the energy of the photon.

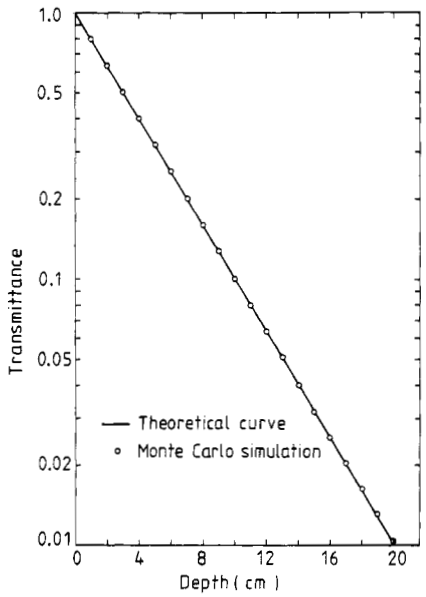

Figure 2. Comparison of results of Monte Carlo simulation with the theoretical curve for exponential attenuation of a 60 keV monoenergetic x-ray beam in Lucite. Number of incident photons, 10^5.

The sampling procedure simulates the attenuation of a primary beam in a narrow beam geometry in the phantom. An example for a pencil beam of 60 keV photons incident on Lucite is shown in figure 2. The solid line is the expected survival probability, and the points are the Monte Carlo results for 10^5 samples. A linear least-square fit to the points yields a slope, i.e., $-\mu$, of -0.228, as compared to the input value of -0.229.

† The Monte Carlo sampling techniques, such as the inversion method and the rejection method, have been documented by a number of authors, e.g., Hammersley and Handscomb (1964), Raeside (1976).

The interaction site is calculated from the free path length and the incident direction, as will be described in section 2.6. Once it is determined that an interaction occurs inside the phantom, one of the three interaction processes is selected by random sampling according to the relative cross-sections of the processes at the appropriate photon energy.

2.2. Photoelectric effect

If the photoelectric effect is chosen, the photon is assumed to be totally absorbed at the interaction site. Fluorescence x-rays are not traced because the atomic numbers Z of the elements in materials equivalent to soft tissue, such as water or Lucite, are low. The fluorescence yields of these low-Z elements are small, and the energies of the fluorescence x-rays are below 5 keV,† which is chosen to be the cut-off energy in our calculations of photon histories. Therefore, a photon history ends after the first photoelectric event.

2.3. Coherent scattering

If coherent scattering occurs, the scattered photon retains its original energy, and no energy is deposited. The scattering angle θ of the photon, defined as the angle between the direction of flight before and that after the interaction, is sampled from the differential cross-section of coherent scattering for a molecule of the scattering medium:

$$\frac{d\sigma_{coh,m}}{d\Omega} = \frac{d\sigma_{Th,e}}{d\Omega} \cdot F_m^2(v^2)$$
$$= \tfrac{1}{2} r_0^2 (1+\cos^2\theta) F_m^2(v^2) \qquad (2)$$

where r_0 is the classical electron radius, $d\Omega = 2\pi \sin\theta \, d\theta$ is the solid-angle element, $d\sigma_{Th,e}/d\Omega$ is the Thomson differential cross-section per electron, and $F_m^2(v^2) = \sum_{i=1}^{N} n_i F_i^2(v, Z_i)$ is the square of the form factor of a molecule, which one obtains by assuming that the coherent cross-sections of individual atoms combine independently. N is the number of different kinds of atoms, and n_i is the number of atoms of the same kind in the molecule. The variable v combines the dependence of the form factor on the scattering angle and the photon energy E:

$$v = \frac{\sin(\theta/2)}{\lambda} = 29.1433 \left(\frac{E}{m_0c^2}\right)(1-\cos\theta)^{1/2} \text{ Å}^{-1}.$$

It varies from zero at $\theta = 0$ to the maximum value $\bar{v}$ at $\theta = \pi$ such that $\bar{v} = 29.1433 (E/m_0c^2)\sqrt{2}$ for a given E, where m_0c^2 is the rest mass energy of an electron.

The square of the atomic form factor, $F_i^2(v, Z_i)$, is the probability that the Z electrons of the atom take up a recoil momentum without absorbing any energy. The atomic form factors have been tabulated in the literature (Hanson *et al* 1964, Cromer and Waber 1974, Hubbell and Øverbø 1979). For a given Z_i, $F_i(v, Z_i)$ decreases rapidly from a maximum value of Z_i to zero as v increases from zero to infinity. Thus, the differential cross-section of coherent scattering is strongly peaked in the forward direction, especially for high-energy photons and low-Z elements. These trends can

† Note that the mean free path of a 5 keV photon in water is about 0.24 mm; this is much smaller than the dimensions of the area or volume elements used in our calculations.

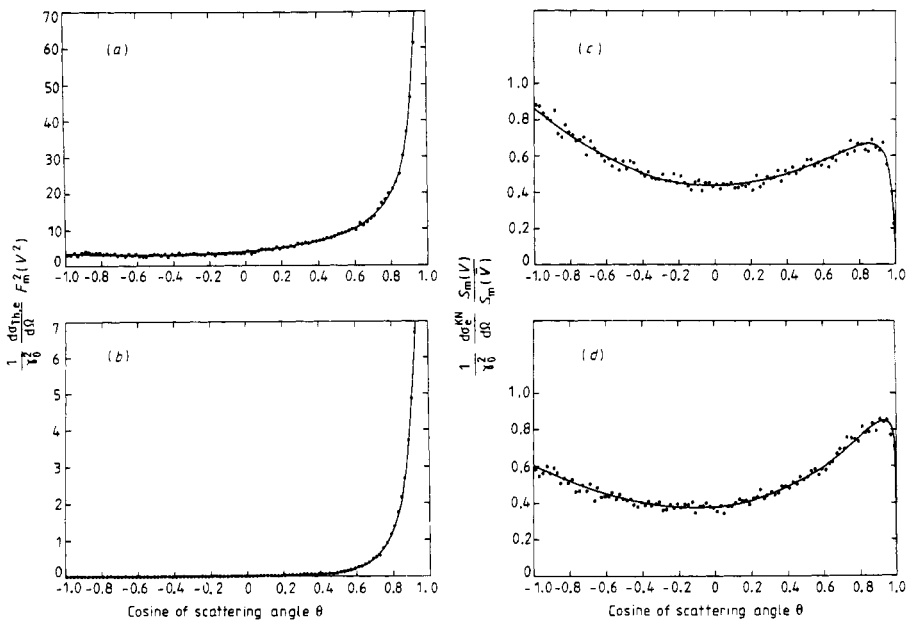

Figure 3. Comparison of results of Monte Carlo simulation (dots) with theoretical angular distributions (solid line) for coherent scattering at photon energies of (*a*) 20 keV and (*b*) 80 keV, and for incoherent scattering at photon energies of (*c*) 20 keV and (*d*) 80 keV; all in Lucite, and 10^5 samplings in each case.

be observed in figures 3(*a*) and (*b*), in which we plotted the differential cross-sections for Lucite at 20 keV and 80 keV, respectively.

Since the area under the curve of $d\sigma_{coh,m}/d\Omega$ is small compared with the area of the smallest rectangle that can enclose this curve, the efficiency of sampling, i.e., the probability that a sample is to be accepted, will be very low if one uses the rejection method to obtain random samples from this function. In our calculations, therefore, we chose the generalised rejection method suggested by Carter and Cashwell (1975). In this method, $d\sigma_{coh,m}/d\Omega$ is regarded as the product of two PDFs, $f_1(v^2) = (1/r_0^2)(d\sigma_{Th,e}/d\Omega)$ and $f_2(v^2) = F_m^2(v^2)/I(\bar{v}^2)$, where $f_1(v^2)$ is normalised to a maximum of unity and $I(v^2) = \int_0^{v^2} F_m^2(v^2)\,dv^2$. A random sample is first obtained with the inversion method from the cumulative distribution function of $f_2(v^2)$, $\int_0^{v^2} f_2(v^2)\,dv^2 = I(v^2)/I(\bar{v}^2)$; this v^2 is then accepted with probability $f_1(v^2)$. $I(v^2)$ can be derived by numerical integration from the tabulated form factors. It is important to note that, for a given material, $I(v^2)$ depends only on v^2, but not on the photon energy or the scattering angle independently. Therefore, only one table of $(I(v^2), v^2)$ pairs from $v^2 = 0$ up to the value of $\bar{v}^2$ corresponding to the maximum energy of interest needs to be stored in the computer. For a given E, one can calculate $\bar{v}^2$ and determine $I(\bar{v}^2)$ from the table by linear interpolation. A random sample of v^2 is then given by another linear interpolation from the inverse table $(v^2, I(v^2))$, such that $v^2 = I^{-1}(\xi \cdot I(\bar{v}^2))$, where ξ is a random number.

Figures 3(*a*) and (*b*) show the differential cross-sections of coherent scattering in Lucite, plotted as a function of $\cos\theta$. The solid curves are calculated from equation (2) scaled by $1/r_0^2$. The points are random samples which we obtained by use of the generalised rejection technique described above. It is apparent that, except for statistical fluctuations, the Monte Carlo samples closely follow the theoretical curves.

These results verify that our Monte Carlo sampling scheme can generate scattering angles for coherent scattering events according to the physical model. The efficiency of this sampling scheme depends on the photon energy and the material. For Lucite, the efficiencies are about 78% and 94% at 20 keV and 80 keV, respectively.

2.4. Incoherent scattering

In an incoherent scattering process, a photon collides with an atomic electron and imparts some of its energy and monentum to the struck electron, the photon being deflected from its original direction of flight. The energy of the scattered photon, E', as derived by Compton, is

$$E' = E/[1 + (E/m_0c^2)(1 - \cos\theta)]. \tag{3}$$

Hence, by the law of conservation of energy, the kinetic energy of the recoil electron is given by the difference between E and E'.

The maximum energy transferred to the electron in Compton scattering of a 100 keV incident photon is about 28 keV, corresponding to an electron range of only about 13 μm in water (Evans 1972). The energy of the recoil electron is therefore assumed to be absorbed at the interaction site. Furthermore, if the energy of the scattered photon is less than 5 keV, the cut-off energy for our calculations, the photon is assumed to be absorbed locally, and the photon history is terminated.

The differential cross-section of incoherent scattering is governed by the Klein–Nishina formula, modified by the incoherent scattering function:

$$\begin{aligned} \mathrm{d}\sigma_{\mathrm{incoh,m}}/\mathrm{d}\Omega &= (\mathrm{d}\sigma_{\mathrm{e}}^{\mathrm{KN}}/\mathrm{d}\Omega)S_m(v) \\ &= \frac{r_0^2}{2}\left(\frac{E'}{E}\right)^2\left(\frac{E'}{E} + \frac{E}{E'} + \cos^2\theta - 1\right)S_m(v). \end{aligned} \tag{4}$$

The Klein–Nishina formula was derived for the interaction of a photon with a free electron. $S_m(v) = \Sigma_{i=1}^{N} n_i S_i(v, Z_i)$ is the incoherent scattering function for a molecule of the scattering medium, assuming that atomic cross-sections are additive. The incoherent scattering function of an atom, $S_i(v, Z_i)$, represents the probability that an atom will be raised to any excited or ionised state when a photon imparts a recoil momentum to an atomic electron. It thus takes into account the effect of electron binding on the differential cross-section of incoherent scattering.

The incoherent scattering functions have been tabulated in the literature for all elements (Cromer and Mann 1967, Cromer 1969, Hubbell *et al* 1975). $S_i(v, Z_i)$ increases rapidly, especially for low-Z elements, at small values of v and approaches a maximum value of Z_i at large v. Therefore, the incoherent scattering function modifies the Klein–Nishina cross-section most prominently for small-angle scattering of low-energy photons in high-Z elements, i.e., under conditions where the effect of electron binding is strong.

In our Monte Carlo program, $\mathrm{d}\sigma_{\mathrm{incoh,m}}/\mathrm{d}\Omega$ is considered to be the product of two PDFs, $g_1(\cos\theta) = (1/r_0^2)\,\mathrm{d}\sigma_{\mathrm{e}}^{\mathrm{KN}}/\mathrm{d}\Omega$ and $g_2(v) = S_m(v)/S_m(\bar{v})$, which are normalised to a maximum of unity. For a given photon of energy E, a sample of $\cos\theta$, and hence the corresponding values of E' and v, is first determined by a rejection technique† from $g_1(\cos\theta)$; this v is then accepted with probability $g_2(v)$. It should be noted that, since

† The efficiency of the rejection technique for the Klein–Nishina formula decreases with increasing energy. Therefore, for high-energy photons, other sampling methods (e.g., Kahn 1956, Everett *et al* 1971) may be preferred.

$S_m(v)$ for a given material depends only on v, the method requires only one table of $(S_m(v), v)$ pairs to be stored in the computer for all photon energies and scattering angles.

Figures 3(*c*) and (*d*) demonstrate the differential cross-sections of incoherent scattering in Lucite at photon energies of 20 keV and 80 keV, respectively. The sharp drop of the cross-section in the forward direction illustrates the electron-binding effect when the energy transferred to the electron is small. It is apparent that the angular distributions obtained by random sampling agree closely with the theoretical curves. This comparison verifies that our method can generate samples of scattering angles in an incoherent scattering process which are in accord with the theoretical distributions. The efficiency of the sampling scheme used depends on the photon energy and the material. For the two examples shown here, the efficiencies are about 56% and 51%, respectively.

2.5. Determination of the azimuthal angle

The azimuthal angle ψ in coherent or incoherent scattering is uniformly distributed in the angular interval $(-\pi, \pi]$ because all directions around the initial line of flight of the incoming photon are equally probable. Since $\sin\psi$ and $\cos\psi$ are the relevant quantities to be used in the calculation of the interaction site of the photon, we employed a two-dimensional generalised rejection technique (Von Neumann 1951) which can determine $\sin\psi$ and $\cos\psi$ directly. In this method, a pair of random numbers (ξ_1, ξ_2) is generated and transformed linearly to a point (x, y) on the x-y plane, where $x = 2\xi_1 - 1$, $y = 2\xi_2 - 1$. The points outside the unit circle centred at the origin, i.e., $x^2 + y^2 > 1$, are rejected. The points retained are then uniformly distributed inside the unit circle, and therefore

$$\sin\psi = \frac{2xy}{x^2 + y^2} \tag{5}$$

and

$$\cos\psi = \frac{x^2 - y^2}{x^2 + y^2} \tag{6}$$

correspond to the sine and cosine of an azimuthal angle uniformly distributed in $(-\pi, \pi]$. This method does not involve the calculation of trigonometric functions or square roots; it is thus more efficient in terms of computer time than other methods which determine ψ only.

We have compared the distribution of azimuthal angles, obtained by the two-dimensional generalised rejection technique, with the uniform distribution. It is confirmed that the relative sampling frequency of the azimuthal angle is uniform over the range $-\pi < \psi \leq \pi$ except for the small variation around the expected constant value which is caused by the inherent statistical fluctuations.

2.6. Determination of the interaction site

The coordinates of all collision sites are calculated with reference to a fixed coordinate system whose origin is located on the surface of the scattering medium and whose z-axis coincides with the central ray of the incident beam. If the nth collision which the photon undergoes is a scattering process, either coherent or incoherent, and if

the deflection angle and the azimuthal angle after the scattering have been determined by the methods discussed in the preceding sections, the site of the $(n+1)$th collision can be derived in terms of the known quantities. For convenience, a primed coordinate system displaced translationally from the fixed coordinate system and with its origin at the nth collision site is introduced. The geometrical relationships of these quantities are illustrated in figure 4. By using these relationships, one can derive (Chan 1981) θ_{n+1} and ϕ_{n+1} in terms of θ_n, ω_{n+1}, ψ_{n+1} and ϕ_n; the $(n+1)$th collision site with reference to the unprimed coordinate system is then given by

$$x_{n+1} = x_n + \rho_{n+1} \sin\theta_{n+1} \cos\phi_{n+1} \tag{7}$$

$$y_{n+1} = y_n + \rho_{n+1} \sin\theta_{n+1} \sin\phi_{n+1} \tag{8}$$

$$z_{n+1} = z_n + \rho_{n+1} \cos\theta_{n+1}. \tag{9}$$

These coordinates, together with the geometry of the phantom, determine whether the $(n+1)$th collision can occur inside the phantom. They also specify the site of energy absorption in the phantom in case the $(n+1)$th interaction event is due to the photoelectric effect or incoherent scattering.

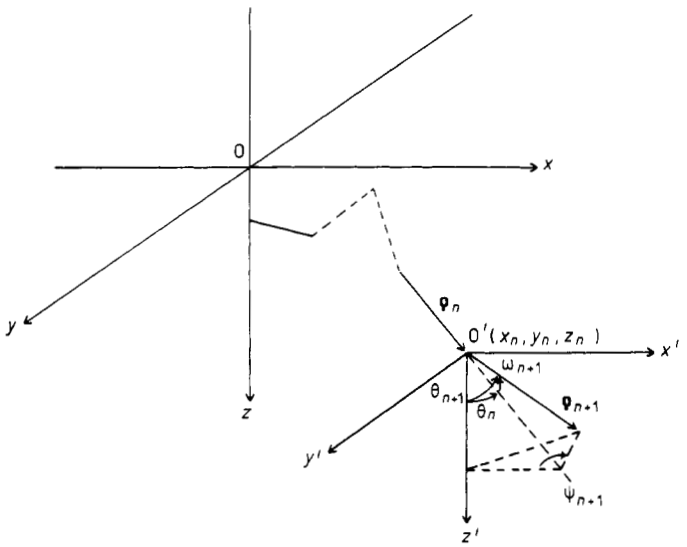

Figure 4. Coordinate systems and quantities used for the determination of interaction sites of a photon in a scattering medium. (x_n, y_n, z_n) are the coordinates of the nth collision site with reference to the unprimed coordinate system, $\hat{\rho}_n$ is a unit vector, $\hat{\rho} = \boldsymbol{\rho}/\rho$, in the direction of flight of the photon after the $(n-1)$th scattering, ρ_n is the free path length between the $(n-1)$th and nth collisions, θ_n is the angle between $\hat{\rho}_n$ and $\hat{z}$ after the $(n-1)$th scattering $(0 < \theta_n \leq \pi)$, ϕ_n (not shown) is the azimuthal angle relative to the x-axis after the $(n-1)$th scattering $(-\pi < \phi_n \leq \pi)$, ω_{n+1} is the deflection angle in the nth scattering, i.e., the angle between $\hat{\rho}_n$ and $\hat{\rho}_{n+1}$, and ψ_{n+1} is the azimuthal angle in the nth scattering, defined to be the angle between the plane formed by $\hat{\rho}_n$ and $\hat{\rho}_{n+1}$ and the plane formed by $\hat{\rho}_n$ and $\hat{z}'$.

If a primary or scattered photon penetrates the phantom and impinges on the image plane, the probability of energy deposition in the screens is derived analytically from the energy and direction of each individual photon incident on the screens, and from the coating density, the mass energy absorption coefficients, and the total mass attenuation coefficients of the screen phosphor material. For incident energies above the K edge of the high-Z element in the phosphor material, the reabsorption of the

K-fluorescence radiation emitted from the high-Z element is included in the calculation of x-ray energy absorption by use of the K-reabsorption factor (Chan 1981, Chan and Doi 1983). Other secondary processes are neglected.

We have previously discussed the relationship between the x-ray energy absorbed in the screen phosphor and radiographic film density (Chan 1981, Chan and Doi 1983). We deduced that the film density is related to the x-ray energy absorbed in the phosphor by the characteristic curve of the film. This simple sensitometric relationship allows a theoretical prediction of the screen–film system response to radiation by calculation of the energy deposited in the screens.

3. Calculation of scatter fractions

Figure 5 illustrates the geometry used in the Monte Carlo calculations. A pencil beam of photons impinged normally on the surface of a homogeneous Lucite phantom. The phantom was infinite in area and uniform in thickness. A pair of screens was placed parallel to the exit surface of the phantom.

For comparison with experimental data, polyenergetic x-rays were used as the input spectra. The spectra were measured with a high-purity germanium spectrometer system in our laboratory (Chan 1981). The x-ray source was a Siemens 150/30/50R tungsten-anode tube with a Siemens Tridoros 150G-3 generator. The linear attenuation coefficients for the photoelectric effect, incoherent scattering, and coherent scattering in Lucite are plotted in figure 6. They were computed from the elemental cross-section data tabulated by Storm and Israel (1970). For photon energies above

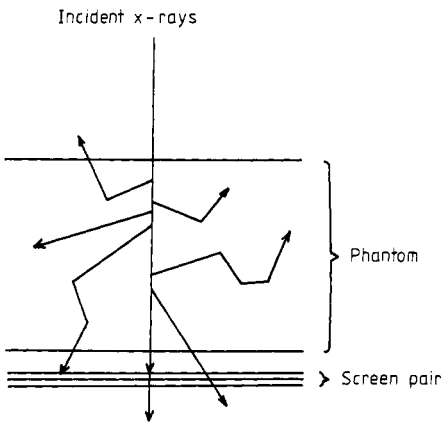

Figure 5. Geometrical model used in the Monte Carlo calculations: A pencil x-ray beam impinges normally on the surface of a plane parallel phantom of infinite area. A pair of screens is used as the recording system.

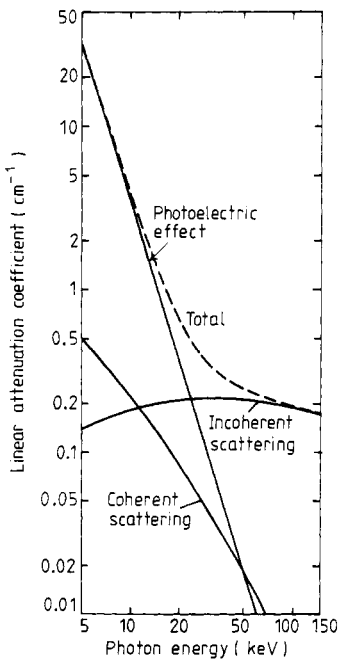

Figure 6. Linear attenuation coefficients for photon interactions in Lucite, $(C_5H_8O_2)_n$, density 1.19 g cm^{-3}.

25 keV, Compton scattering is the most probable interaction process, accounting for the large scattering component involved in x-ray diagnostic examinations.

We included nine recording systems in the calculations in order to study the effect of detector response on the imaging properties of scattered radiation. One of these is a perfect-absorption system, which was assumed to absorb all photons incident on the image plane. We chose eight different screens which contain six different phosphor materials—Detail, Par Speed, Hi-Plus ($CaWO_4$), Quanta II (BaFCl), Quanta III (LaOBr), Lanex Regular (Gd_2O_2S), X-Omatic Regular ($BaSrSO_4$) and B G Mid Speed (Y_2O_2S/Gd_2O_2S) systems. These phosphor materials represent the typical phosphors used in commercial fluorescent screens.

The Monte Carlo program traced the path of each individual photon. If a photon penetrated the phantom in the forward direction, the probability and location of energy deposition in the screens were determined from the exit polar angle and coordinates of the photon. The spatial distribution of the scattered radiation, which can be called the point spread function† recorded on the screen–film system, PSF (x, y), was determined as follows. Since both the phantom and the recording system were isotropic, the spatial distribution of energy absorption in the screens would also be rotationally symmetric. It was therefore convenient to choose the area elements on the image plane to be concentric rings centred at the transmitted primary ray. A radial width of 2 mm, which was much larger than the mean free paths of the energetic electrons released in the photoelectric or Compton process in the screens under diagnostic conditions, was chosen for the rings. The total energy absorbed in each area element was computed. In the central ring, the energy absorbed due to the primary and the scattered photons was determined separately. The energy density at a radial distance from the centre was obtained as the energy absorbed per unit area in the corresponding area element. The spatial distribution of the energy density due to scattered radiation absorbed in the screens per unit absorbed primary radiation corresponded to the point spread function.

The scattered radiation, $i_s(x, y)$, absorbed in the image plane for an extended incident field of area A is given by a convolution of the point spread function with the intensity distribution, $i_p(x, y)$, of the transmitted primary radiation recorded on the same screens:

$$i_s(x, y) = \iint_A \text{PSF}\,(x - x', y - y') i_p(x', y')\,dx'\,dy'. \tag{10}$$

For a uniform, infinitely broad and parallel primary beam, equation (10) can be simplified to an integration of the point spread function, multiplied by the intensity i_p of the transmitted primary radiation absorbed on the screens. Thus, i_s is independent of the position (x, y):

$$\begin{aligned} i_s &= i_p \int_{-\infty}^{\infty}\int \text{PSF}\,(x - x', y - y')\,dx'\,dy' \\ &= i_p \int_{-\infty}^{\infty}\int \text{PSF}\,(x', y')\,dx'\,dy'. \end{aligned} \tag{11}$$

† Note that the point spread function of scattered radiation defined here is different from the conventionally defined point spread function, the volume of which is normalised to unity.

If the variable is changed to the radial distance r, equation (11) becomes

$$i_s = i_p \int_0^\infty \mathrm{PSF}\,(r) 2\pi r \, dr. \tag{12}$$

The scatter function, F, recorded on a screen–film system is defined as the ratio of the absorbed scattered radiation to the total absorbed radiation:

$$F = \frac{i_s}{i_s + i_p}. \tag{13}$$

To derive the scatter fraction from an incident pencil beam as used in the computer simulation, we obtained i_s from a summation of the energy deposited by all scattered photons, whereas i_p was the energy deposited in the screens by the transmitted primary beam.

Figure 7 shows the scatter fractions calculated at different thicknesses of Lucite for the nine recording systems with an 80 kV incident spectrum. Except for the results obtained with a 20 cm thick Lucite phantom, the values are the averages for 10 runs, each with 10^4 incident photons. Twenty runs were used for the 20 cm phantom. The standard deviation of the mean scatter fractions is less than 1%. This standard deviation accounts for only the statistical uncertainty of the Monte Carlo calculations. As can be seen from the figure, the scatter fraction increases rapidly as the thickness of the scattering medium increases. For Lanex Regular screens, it is 88% for the 20 cm thick phantom, resulting in only 12% of the image contrast that would be achieved in a scatter-free situation.

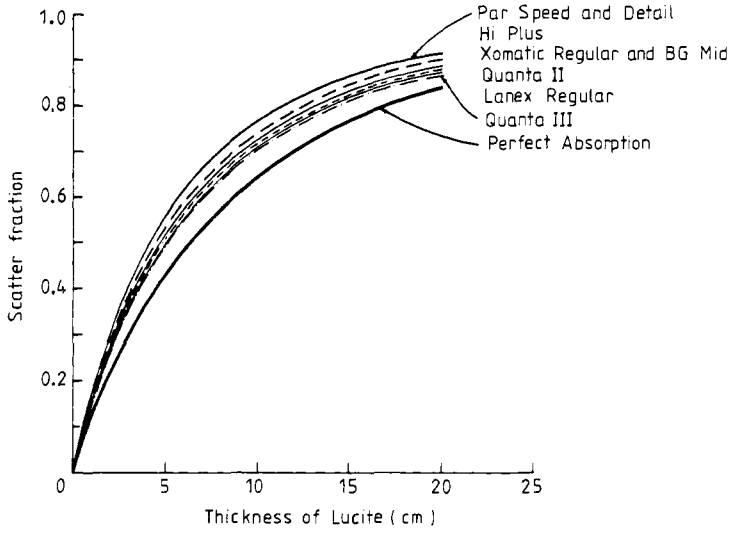

Figure 7. Dependence of the scatter fraction on thickness of the Lucite phantom for an 80 kV incident beam and nine different recording systems. The scatter fractions were determined with Monte Carlo calculations.

The recorded scatter fractions depend on the screens used. This dependence is caused primarily by the difference in the energy response, which is due to the atomic composition, and the coating density of the screen phosphors. For calcium tungstate

screens, the K edge occurs at 69.5 keV and therefore relatively few photons in the 80 kV spectrum possess energies above the tungsten K edge. The relatively higher transparency to primary photons is responsible for the fact that the scatter fractions are larger than those obtained with the other screens, which contain K edges at lower energies. The relative sensitivity of the screens to scattered radiation thus varies with the incident x-ray energy. At 80 kV, the Par Speed and Detail systems are the most susceptible to the effects of scattered radiation, whereas the Lanex Regular and Quantum III systems are less susceptible.

For screens of the same phosphor material, the thicker the screens are, the lower the scatter fractions they detect, since the absorption of scattered radiation in the screens increases less rapidly than does the absorption of primary photons when the thickness of the phosphor increases. The perfect-absorption detector records the lowest scatter fractions. This can be explained by the fact that, in screens of finite thickness, a smaller proportion of primary photons than scattered photons is absorbed due to the higher penetrating power and shorter path length of the primary component in the screens. In a perfect-absorption detector such as a thick NaI crystal, this differentiation in the absorption of scattered and primary components is eliminated.

4. Measurement of scatter fractions

Scatter fractions were measured with the experimental set-up shown in figure 8. Lucite blocks 50×50 cm^2 in area and 2.5 cm in thickness were used as the scattering medium. To obtain a desired total thickness, we combined an appropriate number of these blocks. The Lucite phantom was supported by four adjustable screws on a heavy platform, so that the spacing between the Lucite and the platform could be varied. The surface of the platform was covered with a thick layer of lead which reduced the backscatter. The screen–film system contained in a cassette was centred on the platform under the phantom. A phantom-to-film spacing of 2.5 cm was used in this study.

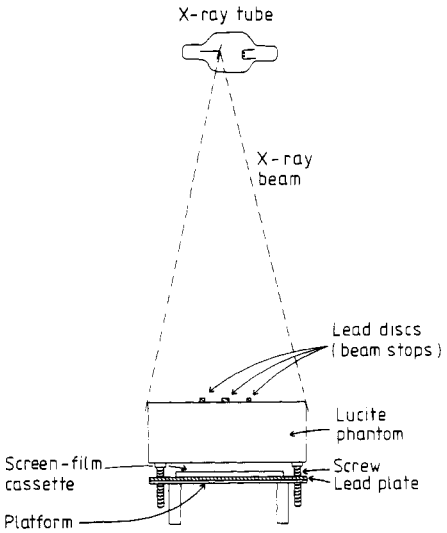

Figure 8. Experimental set-up for the measurement of scatter fractions.

To measure the scatter fractions, we placed six lead discs, 4 mm thick and ranging from 2.5 mm to 10 mm in diameter, on top of the Lucite. These lead discs were thick enough to prevent the primary beam from reaching the screen. Therefore, the film density behind the discs was caused by scattered radiation alone, whereas the film density outside the disc images was caused by both primary and scattered radiation.

The lead discs were positioned evenly on the circumference and also at the centre of a circle which was about 10 cm in diameter. The minimum distance between two lead discs was approximately 5 cm, and the distance from any lead disc to the closest edge of the phantom was about 20 cm. With this arrangement, the change in the amount of scattered radiation under a beam stop due to the presence of the other beam stops should be negligible, because the portion of the surrounding area covered by the other beam stops was much smaller than the irradiated area. However, the amount of scattered radiation recorded at the centre of each disc image was reduced, since the disc blocked a column of primary radiation from entering the phantom above the disc image. Consequently, the scatter fraction measured with each of the six discs decreased with increasing disc diameter. The scatter fraction for a uniformly irradiated phantom could be obtained by extrapolation from these six values to zero disc area.

The radiation source was a Siemens Bi 125/3/50 RG microfocus tungsten-anode tube with a Tridoros 150G-3 three-phase twelve-pulse x-ray generator. A focal spot of 200 μm nominal size was used for the exposures. The focal spot to film distance was 200 cm. The whole surface area of the Lucite phantom was irradiated. This geometry yielded a maximum obliquely incident angle of less than 8 deg. The incident radiation was therefore assumed to be approximately a parallel beam.

With the small spacing from the phantom to the film and the large distance from a beam stop to the edge of the phantom, the experimental set-up just described would be a good approximation to the geometry used in the Monte Carlo calculations, which simulated a uniform parallel x-ray beam incident on a phantom of infinite area, since the tail of the point spread function for radial distances larger than 20 cm contains a negligible amount of energy under diagnostic imaging conditions.

In the measurements, the thickness of the Lucite phantom was varied from 2.5 cm to 20 cm in increments of 2.5 cm. The six lead discs were placed in contact with the phantom surface in all exposures. For each Lucite thickness, three films of slightly different background densities, in the range of 1.8 to 2.5, were exposed. Three additional films were exposed with the phantom removed and with the lead discs supported in air at their same locations by a piece of film base mounted on a supporting frame. In this way, we were able to estimate the scattered radiation from the surroundings other than the phantom. The main source of this scatter component was the backscattered radiation from the cassette. The characteristic curve of the screen–film system was produced with an inverse-square intensity-scale sensitometer (Haus and Rossmann 1970). The film samples and the sensitometry strip were developed at the same time in a Kodak M-6 X-Omatic film processor.

Film densities were measured with a Macbeth TR 524 transmission densitometer. For each disc image, the density at the centre of the beam stop and at eight points around the disc image were measured. The density outside the disc image was taken as the average of the eight readings. The sensitometric curve was also measured with the densitometer and was smoothed by least-squares curve-fitting with discrete Legendre polymonials (Chan and Doi 1978). The film densities both inside and outside the disc images were converted to relative absorbed energy in the screens by means of the same characteristic curve, regardless of differences in the spectral distribution

of the radiation causing the film density in these areas. This is justified since, as was discussed by Chan (1981), a family of energy-dependent characteristic curves is reduced to one curve when the abscissa is expressed in terms of absorbed energy rather than of exposure. Since the exposure outside the beam stop was caused by both primary and scattered radiation, whereas the exposure under the beam stop was caused by scattered radiation alone, the ratio of the absorbed energy in the centre of the disc image to the absorbed energy outside corresponded to the scatter fraction measured at this diameter of the beam stop. The scatter fractions measured for each beam stop of the same diameter and recorded on the three films were averaged. The same procedure was carried out on the corresponding three films which were exposed without the Lucite phantom. We assumed that the scattered radiation on the former three films was composed of scattered radiation from the phantom and from the surroundings, and that the latter films recorded only the scattered radiation from the surroundings. The scatter fraction due to the phantom alone was therefore obtained by subtraction of the scatter due to the surroundings from the total value. Finally, the scatter fraction for an unperturbed beam, i.e., the value measured with a zero-area beam stop, was derived by linear extrapolation of the six corrected fractions versus the area of the beam stops.

It is difficult to analyse the propagation of errors in the complicated procedures just described for the determination of the scatter fraction. Therefore, we examined the reproducibility of the results in order to obtain an estimation of the experimental uncertainty. The measurement of the scatter fractions at six different thicknesses of Lucite was repeated seven times with the Par Speed/XRP system as the recording system. The standard deviation of one measurement, as estimated from these results, was 0.015. Since all scatter fractions were determined with similar procedures, it is expected that a standard deviation of this magnitude would be applicable to all results.

5. Comparison of experimental scatter fractions with Monte Carlo results

5.1. Dependence on recording system

In the first series of experiments, the scatter fractions were measured as a function of Lucite thickness with eight different screens. Kodak XRP film was combined with the screens, except for the Lanex Regular system, with which the green-sensitive Kodak OG film was used. The tube voltage was fixed at 80 kV. Exposures were made with the screen and film contained in a vacuum cassette. The casette had an aluminum backing and a thin plastic surface which was practically transparent to x-rays.

The scatter fractions were calculated with the Monte Carlo program under input conditions which corresponded to the experiments. Figure 9 shows a comparison between the calculated and experimental results for the Par Speed/XRP and Lanex Regular/OG systems. It is evident that the scatter fractions calculated by Monte Carlo simulation agree closely with the experimental data. The measured scatter fractions for the other six screens were plotted against the calculated results as shown in figure 10. The scatter fractions were determined for Lucite thicknesses between 2.5 cm and 20 cm. The diagonal straight line indicates the curve expected if the calculated scatter fractions are exactly the same as the measured values. It is apparent that the data points agree with the expected curve within the experimental standard deviation of 0.015 for all of the screen–film systems.

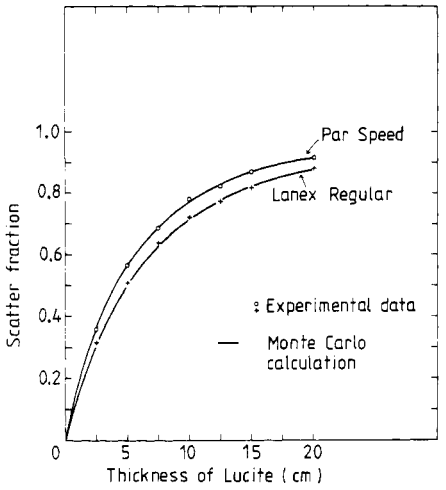

Figure 9. Comparison of measured scatter fractions with results of Monte Carlo calculations for Par Speed and Lanex Regular screens. The scatter fractions were determined for Lucite phantoms irradiated with an 80 kV x-ray beam.

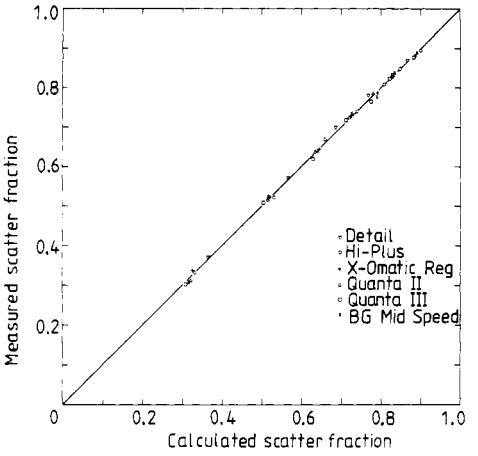

Figure 10. Comparison of measured scatter fractions with results of Monte Carlo calculations for six screens: Detail, Hi-Plus, Quanta II, Quanta III, X-Omatic Regular, and B G Mid Speed. The scatter fractions were determined for Lucite phantoms of thicknesses between 2.5 cm and 20 cm. The incident spectrum was 80 kV. Vacuum cassette.

The results of these comparisons support the validity of our Monte Carlo simulation; they also indirectly verify the simple conversion relationship between film density and energy absorbed in the screens which was assumed in the calculations. It will be noted from these results that both our Monte Carlo simulation and our experimental approach can distinguish differences in the scatter fractions due to the use of different screens.

5.2. Dependence on energy of incident spectrum

Scatter fractions at tube voltages of 60 kV, 80 kV, 100 kV, and 120 kV were measured as a function of Lucite thickness. Par Speed screens with XRP film in a vacuum cassette were used as the recording system. Figure 11 compares the measured and calculated scatter fractions for the 60 kV, 100 kV, and 120 kV incident beam energies; the results at 80 kV are included in figure 9. The curves are Monte Carlo results, and the points are experimental values. It can be seen that the scatter fractions increased slightly with tube voltage. The increase was approximately 0.02 to 0.03 from 60 kV to 80 kV, depending on the Lucite thickness, and less than 0.01 from 80 kV to 120 kV. The experimental results agree closely with the calculated values for the 80 kV, 100 kV, and 120 kV beams. For the 60 kV incident beam, the measured scatter fractions were about 0.01 higher than the calculated values. However, if we consider the several factors which affect the accuracy of the two approaches, namely the experimental errors in scatter fraction measurements, the uncertainty in the cross-section data for the Monte Carlo calculation, and the possible difference in the incident x-ray spectra used for the experiment and the simulation, the agreement is satisfactory. The results of these comparisons therefore support the validity of the Monte Carlo simulation for different incident spectra in the diagnostic energy range.

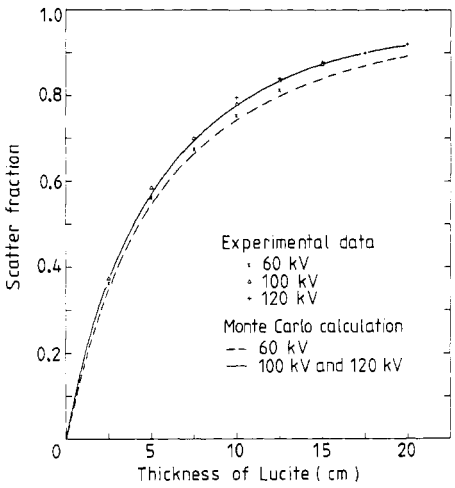

Figure 11. Comparison of measured scatter fractions with Monte Carlo results for 60 kV, 100 kV, and 120 kV incident beams. The scatter fractions were determined for Lucite phantoms of thicknesses between 2.5 cm and 20 cm. Par Speed screens in a vacuum casette were used as the recording system.

6. Edge response of scattered radiation

The point spread function of the scattered radiation from a homogeneous phantom, recorded on a screen–film system, is assumed to be rotationally symmetric. Hence the corresponding line spread function can be obtained from a one-dimensional integration along any axis of this isotropic point spread function. If the point spread function, PSF(x, y), is integrated along the y-axis, the line spread function, LSF(x, y), is given by

$$\mathrm{LSF}(x) = \int_{-\infty}^{\infty} \mathrm{PSF}\,(x, y)\,\mathrm{d}y$$

$$= 2 \int_{r=x}^{\infty} \frac{\mathrm{PSF}(r) r\,\mathrm{d}r}{(r^2 - x^2)^{1/2}}. \tag{14}$$

Direct determination of the line spread function with the slit method is usually impractical because of the very broad and low-intensity distribution of the scattered radiation. An alternative approach is to measure the edge response and to derive the line spread function by numerical differentiation; however, this can cause large fluctuations. For comparison, the line spread function obtained by Monte Carlo simulation was integrated to yield the edge distribution, which was then compared with the experimentally measured edge response.

To determine the edge response of scattered radiation, we assumed that the radiation incident on the scattering medium is a step function of intensity i_0:

$$i_e(x) = i_0,\ x \geq 0$$

$$= 0,\ x < 0. \tag{15}$$

The spatial distribution, $E(x)$, recorded on a screen–film system is given by a con-

volution of the transmitted primary radiation, which is a step function of intensity i_p, with the line spread function of the scattered radiation (Doi 1968), yielding

$$E(x) = i_p + i_p \int_{-\infty}^{x} \text{LSF}(x')\,dx',\ x \geq 0$$

$$= i_p \int_{-\infty}^{x} \text{LSF}(x')\,dx',\ x < 0. \tag{16}$$

The screen–film unsharpness was neglected in the derivation of these relations.

The experimental arrangement for the measurement of edge responses was similar to that for the measurement of scatter fractions (figure 8). The lead discs were replaced by a lead plate, the edge of which was aligned with the central ray such that the lead plate shielded one half of the Lucite phantom from the incident radiation. The plate consisted of a 3 mm thick layer of lead supported by a 3 mm thick layer of aluminum. The sharp edge of the lead plate was placed parallel to the tube axis to reduce the non-uniformity of the incident x-ray field due to the Heel effect. With a 200 μm focal spot and a 200 cm focal-spot-to-film distance, the effect of geometric unsharpness on the edge image would be negligible. The spacing between the phantom and the film was fixed at 2.5 cm for all exposures. A vacuum cassette was employed because it provided good contact between the screens and the film. After exposure, the film was developed together with an intensity-scale sensitometry strip.

The edge image and the sensitometric (H & D) curve were scanned with a GAF model 101 one-dimensional microdensitometer. An effective scanning aperture 7 μm in width and 1300 μm in length was used. The output signal of the microdensitometer was recorded on a linear chart recorder and also digitised by an analog-to-digital converter. The analog-to-digital converter was interfaced with a PDP 8/e computer, which stored the discrete output data taken at the sampling distance that had been preset on the interface. For the edge scans, a scanning speed of 10 mm min^{-1} and a sampling distance of 200 μm were chosen. Typically, a distance of 14 cm was scanned for each edge distribution. The H & D curve, scanned with the same microdensitometer settings and smoothed by curve-fitting, was used for conversion of the film density to relative absorbed energy on the screens. The measured edge response was then scaled and compared to the edge distribution predicted by the Monte Carlo simulation. The data analysis procedures, including H & D curve-smoothing, density-to-absorbed-energy conversion, scaling, and comparison, were carried out automatically with the PDP 8/e computer.

The edge responses were measured for various Lucite thicknesses, tube voltages, and screen–film systems. Figures 12(*a*)–(*c*) show the comparisons between the experimental results and the Monte Carlo edge distributions for the Par Speed/XRP system at 5 cm, 10 cm, and 15 cm Lucite thickness, respectively, at 80 kV tube voltage. Figures 13(*a*)–(*c*) illustrate similar comparisons for the Lanex Regular/OG system. The Monte Carlo edge distributions are plotted as solid curves, and the dots are derived from the microdensitometer scans at a 200 μm sampling distance. Both the experimental and calculated distributions are scaled such that the transmitted primary components have unit intensity, which is equal to the magnitude of the discontinuity at the edge boundary. The large fluctuation in the high-density region of the experimental edge distribution is caused mainly by the high electronic noise of the

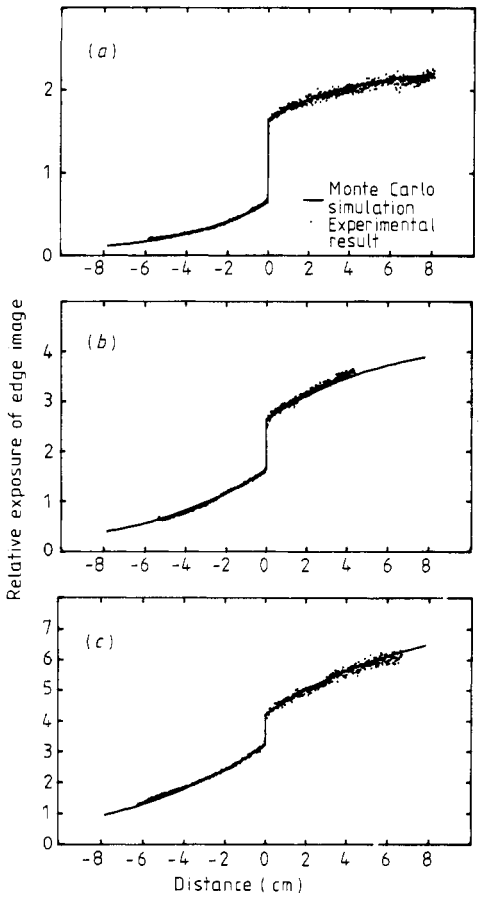

Figure 12. Comparison of measured edge responses of scattered radiation with Monte Carlo results for Par Speed screens. The edge responses were determined for Lucite phantoms of thicknesses (*a*) 5 cm, (*b*) 10 cm, and (*c*) 15 cm irradiated with an 80 kV incident beam.

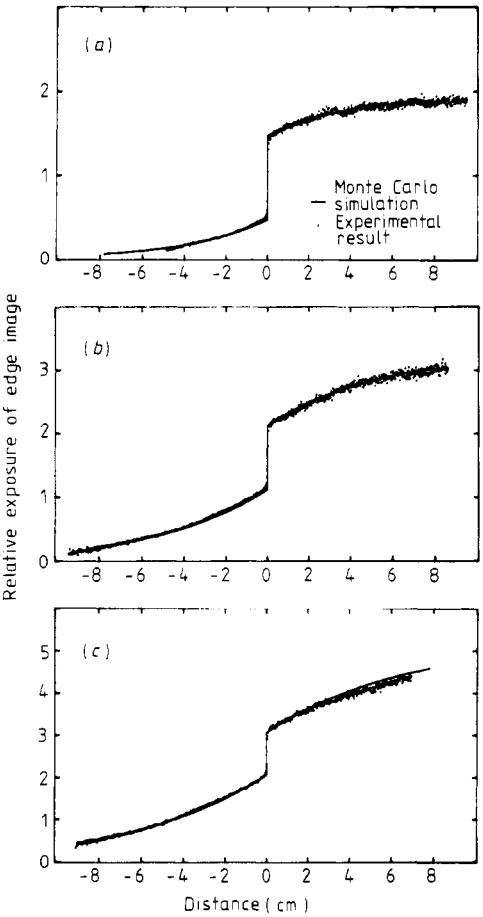

Figure 13. Comparison of measured edge responses of scattered radiation with Monte Carlo results for Lanex Regular screens. The edge responses were determined for Lucite phantoms of thicknesses (*a*) 5 cm, (*b*) 10 cm, and (*c*) 15 cm irradiated with an 80 kV incident beam.

microdensitometer when the light transmission through the film sample is low. It may also be noted that the film graininess increases with density. The density fluctuation is amplified further by the sensitometric conversion, since the gradient of the H & D curve decreases at high densities.

Excellent agreement was observed for both recording systems with the 5 cm thick phantom. For thicker phantoms, the edge image from the low-exposure region to the high-exposure region spans a large density range. Since the slope on the shoulder of the H & D curve tends to be affected more strongly by fluctuations in the exposure and development conditions, the greater uncertainty in the sensitometry may account for the deviation of the measured distribution from the Monte Carlo results in the high-exposure regions. However, in general, the experimental and calculated edge responses agreed very closely in every case, except for some small local deviations. The results of the comparison indicate that the Monte Carlo simulation and the

calculated response of the recording systems can accurately predict the spatial distribution of the scattered radiation.

It is possible to derive the scatter fraction from the edge distribution (Doi 1968). From equations (11), (14), and (16), it follows that

$$\frac{E(\infty)}{i_p} = 1 + \frac{i_s}{i_p} \tag{17}$$

$$\frac{E(0^+)}{i_p} = 1 + \frac{i_s}{2i_p} \tag{18}$$

and

$$\frac{E(0^-)}{i_p} = \frac{i_s}{2i_p}. \tag{19}$$

Hence,

$$\frac{E(\infty) - E(0^+)}{i_p} = \frac{E(0^-)}{i_p} = \frac{i_s}{2i_p}. \tag{20}$$

Therefore, the maximum value on either side of the edge distribution is equal to one half of the scatter-to-primary ratio. The edge response thus provides an estimate of the scatter fraction. However, the uncertainty of this measurement will be large, since it is difficult to determine $E(0^-)$ or $E(0^+)$ accurately because of the data fluctuation on the measured edge image.

7. Discussion and conclusions

Monte Carlo simulation is a practical approach to the study of the physical characteristics of scattered radiation. Once the Monte Carlo program is developed, it is relatively simple, compared to experimental measurements, to perform a systematic investigation of the dependence of the characteristics of scattered radiation on various imaging conditions. The Monte Carlo calculations can also provide results such as the probability of occurrence of the different interaction processes and the distribution of the number of interactions in a photon history, which are difficult—or even impossible—to measure experimentally. However, in a Monte Carlo simulation study, it is of prime importance to test the program thoroughly and to verify the output with sufficient experimental evidence before the results can be accepted as representing the expected physical processes.

In this study, we have demonstrated that the sampling schemes used in our Monte Carlo code can generate random samples from the distribution functions which describe the physical processes of photon interactions. The validity of our Monte Carlo calculations has been verified by comparison with experimental results in various applications. We have shown here that there is close agreement between the results determined by Monte Carlo calculations and by experiments for the scatter fractions and the edge responses of scattered radiation recorded in the image plane for various phantom sizes, x-ray tube voltages, and recording systems. In a previous study, we used the Monte Carlo program to determine absorbed dose and backscatter factors in mammography (Doi and Chan 1980, Chan and Doi 1981, Chan 1981), and we obtained good agreement for comparisons of backscatter factors determined with LiF thermoluminescent dosemeters for four tissue-equivalent phantoms. In a recent study

of the angular and spectral distributions of the scattered radiation transmitted through a phantom under mammographic imaging conditions (Klein *et al* 1981), close agreement was observed between the results predicted by our Monte Carlo calculations and experimental measurements. Furthermore, in a Monte Carlo simulation study of detector responses for x-ray spectrometer systems (Chen *et al* 1980, Chan 1981), good agreement was obtained in the comparisons of detector response curves for both a germanium crystal and a silicon crystal, indicating that our Monte Carlo calculations can accurately simulate the photon interaction processes within the scattering medium. These comparisons thus provide strong evidence in support of the validity of our Monte Carlo calculations.

Finally, it should be noted that results predicted by Monte Carlo simulation contain statistical uncertainties caused by the probabilistic nature of the method as well as potential systematic errors caused by the uncertainties in the input data† and in the physical model of the photon interaction processes. The statistical uncertainties can be reduced by variance-reduction techniques and by an increase in the number of input photons. The systematic errors are difficult to estimate. We have proposed a simulation method to estimate these errors (Chan 1981). However, we did not proceed any further in this direction because it is known that comparison with experimental measurements is a more direct and practical approach to determine the accuracy of the calculated quantities. Based on the close agreement between the experimental results and the Monte Carlo predictions which we obtained, it appears that the Monte Carlo simulation can predict the photon scattering processes accurately and that the potential systematic errors do not bias the results substantially.

Acknowledgments

The authors are grateful to Mrs E F Lanzl for editing the manuscript, and to Mr Scott M Dickerson for secretarial assistance.

This work was supported in part by USPHS Grant CA-24806.

Résumé

La validité d'une simulation de Monte Carlo dans les études du rayonnement diffusé en radiologie diagnostique.

Nous avons développé un programme utilisant la méthode de Monte Carlo pour simuler la diffusion des photons dans des fantômes equivalent-tissu pour des rayons x incidents dans la gamma d'énergie utilisée en diagnostic. Cette étude nous a permis de vérifier que les schémas d'échantillonnages aléatoires en accord avec les distributions de probabilité théorique qui décrivent le processus de diffusion des photons. Le programme de Monte Carlo a été utilisé pour déterminer les fractions diffusées et les réponses des bords pour des fantômes de différentes tailles, énergies de rayons x et systèmes d'enregistrement. Ces qualitées ont été aussi mesurées expérimentalement dans des conditions comparables d'imageries. L'accord entre les résultats prédits et expérimentaux est excellent. Cette étude établit la validité de nos calculs de Monte Carlo pour les études des caractéristiques physiques du rayonnement diffusé en radiologie diagnostique.

† The uncertainties of the tabulated form factors and incoherent scattering functions used in this study were not specified in the references (Hanson *et al* 1964, Cromer and Mann 1967, Cromer 1969, Cromer and Waber 1974). The cross-section data for the three individual processes were stated to be accurate within 3%, and the total cross-section data were accurate within 10% by comparison with measured cross-sections (Storm and Israel 1970).

Zusammenfassung

Die Anwendbarkeit von Monte-Carlo-Simulationen bei der Untersuchung der Streustrahlung in der Röntgendiagnostik.

Unter Verwendung von Monte-Carlo-Methoden wurde ein Computerprogramm entwickelt zur Simulation der Streuung von Photonen in gewebeäquivalenten Phantomen, wobei die Energien der Röntgenstrahlen in einem für die Diagnostik üblichen Bereich lagen. Die Untersuchung bestätigte, daß die im Programm benutzten Probenmethoden Zufallsproben erzeugen in Übereinstimmung mit den theoretischen Wahrscheinlichkeitsfunktionen, die die Photonenstreuprozesse beschreiben. Das Monte-Carlo-Programm wurde angewandt zur Bestimmung der Streuanteile und der Randeffekte für verschiedene Phantomgrößen, Röntgenstrahlenenergien und Aufnahmesysteme. Diese Größen wurden auch experimentell unter vergleichbaren Abbildungsbedingungen gemessen. Zwischen den vorhergesagten und den experimentellen Ergebnissen erhielt man eine hervorragende Übereinstimmung. Diese Untersuchung bestätigt die Gültigkeit unserer Monte-Carlo-Rechnungen über die physikalischen Eigenschaften der Streustrahlung in der Röntgendiagnostik.

References

Barnes G T, Murray Cleare H and Brezovich I A 1976 *Radiology* **120** 691–4
Burgess A E and Pate G 1981 *Med. Phys.* **8** 33–8
Carter L L and Cashwell E D 1975 *ERDA Critical Review Series* TID-26607 (Springfield, VA: NTIS)
Chan H-P 1981 *Ph.D. Dissertation* The University of Chicago
Chan H-P and Doi K 1978 *Med. Phys.* **5** 443–7
—— 1981 *Radiology* **139** 195–9
—— 1983 *Phys. Med. Biol.* **28** to be published
Chen C, Doi K, Vyborny C J, Chan H-P and Holje G 1980 *Med. Phys.* **7** 627–35
Cromer D T 1969 *J. Chem. Phys.* **50** 4857–9
Cromer D T and Mann J B 1967 *J. Chem. Phys.* **47** 1892–3
Cromer D T and Waber J T 1974 *International Tables for X-Ray Crystallography* **4** 71–147
Dance D R 1980 *Phys. Med. Biol.* **25** 25–37
Dick C E, Soares C G and Motz J W 1978 *Phys. Med. Biol.* **23** 1076–85
Doi K 1968 *Jap. J. Non-destructive Inspection* **17** 162–70
Doi K and Chan H-P 1980 *Radiology* **135** 199–208
Evans R D 1972 *The Atomic Nucleus* (New York: McGraw Hill) p 625
Everett C J, Cashwell E D and Turner G D 1971 *USAEC Report* LA-4663
Hammersley J M and Handscomb D C 1964 *Monte Carlo Methods* (London: Methuen)
Hanson H P, Herman F, Lea J D and Skillman S 1964 *Acta Cryst.* **17** 1040–4
Haus A G and Rossmann K 1970 *Radiology* **94** 673–8
Hettinger G and Liden K 1960 *Acta Radiol.* **53** 73–92
Hettinger G and Starfelt N 1959 *Ark. Fys.* **14** 497–511
Hubbell J H and Øverbø I 1979 *J. Phys. Chem. Ref. Data* **8** 69–105
Hubbell J H, Veigele W J, Briggs E A, Brown R T, Cromer D T and Howerton R J 1975 *J. Phys. Chem. Ref. Data* **4** 471–538
Kahn H 1956 *Applications of Monte Carlo* (Santa Monica: Rand) 62–5
Kalender W 1981 *Phys. Med. Biol.* **26** 835–49
Klein D J, Chan H-P, Doi K, Muntz E P, Lee K and Bernstein H 1981 *Med. Phys.* **8** 562 (abstract)
Koblinger L and Zarand P 1973 *Phys. Med. Biol.* **18** 518–31
Levine M M and Hale J 1980 *Phys. Med. Biol.* **25** 545–8
Motz J W and Dick C E 1975 *Med. Phys.* **2** 259–70
Raeside D E 1976 *Phys. Med. Biol.* **21** 181–97
Reiss K H and Steinle B 1973 *Tabellen zur Röntgendiagnostik, Teil II* (Erlangen: Siemens)
Rosenstein M, Prevo F J, Schneider R H, Poston J W and Warner G G 1976 *HEW Publication* (FDA) 76-8030
Storm E and Israel H I 1970 *Nuclear Data Tables* **A7** 565–81
Strid K-G 1976 *Acta Radiol.* Suppl 351
Von Neumann J 1951 *NBS Appl. Math. Series* **12** 36–8
Wilsey R B 1921 *Am. J. Roentgenol.* **8** 328–39